Gyrokinetic particle simulation of electrostatic microturbulence with impurity ions

Xishuo Wei, Hongwei Yang, Shengming Li, Yong Xiao*

Institute for Fusion Theory and Simulation, Department of physics, Zhejiang University, Hangzhou, China

*yxiao@zju.edu.cn

Abstract

Impurity is an important factor that can affect significantly the turbulent transport in tokamaks. In order to study the impurity physics, we implement a new impurity module in the gyrokinetic particle simulation code GTC. With an improved numerical scheme, we expand the validity of the gyrokinetic Poisson equation in the GTC to the short wavelength region, for both non-zonal and zonal part of the perturbed Poisson equation. Verifications of this new scheme is carried out on the linear instability and zonal flow response. The linear simulation of the ion temperature gradient (ITG) instability including the impurity ions shows that the new Poisson solver can obtain the correct linear growth rate and frequency at the thermal ion gyro-radius scale. The residual zonal flow with impurities obtained via the new zonal flow solver is consistent with the numerical and analytical predictions in the large aspect-ratio limit. The nonlinear simulation of the ITG turbulence shows that the turbulent transport is significantly reduced by the impurity ions through decreasing the linear growth rate of the instability.

I. Introduction

Impurity ions exist universally in magnetically confined plasmas, besides majority ions (thermal ions) and electrons. The impurity ions may come from the erosion of the device wall or the plasma sputtering in the divertor. Common kinds of impurity include Carbon, Oxygen and Tungsten. The thermalized alpha particles can also be regarded as one impurity species in the burning D-T plasmas. External impurity injection is observed to lead to long wavelength turbulence suppression, confinement improvement and ion thermal diffusivity reduction in the experiments in TEXTOR-94[1], DIII-D[2, 3], JET[4], and TFTR[5]. Various theories are raised to interpret how the impurity can affect the plasma confinement and transport. As one candidate the impurity mode is excited when the impurity ions have a density profile that increases with the magnetic

flux, in contrast with the thermal ion and electron density profile, even if there is no temperature gradient for thermal ions[6]. In the sheared slab geometry and the long wavelength limit ($k_\perp \rho_i < 1$), analysis shows that this mode can suppress (or enhance) ion temperature gradient (ITG) mode when the impurity ions have the outwardly (or inwardly) peaked density profile[7]. One numerical calculation using the kinetic impurity ions and adiabatic electrons shows that the impurity modes and the ITG mode are strongly coupled and can affect each other significantly[8]. The impurities can also affect various trapped electron modes[9]. A recent research based on the gyrokinetic integral equation and the eigenvalue approach finds that the coupled ITG and TEM can be affected by the impurity ions[10]. Under some special conditions, the impurity acoustic modes coupled with the drift modes can produce an outward transport for the impurity from a quasilinear calculation[11], which is considered to explain the favorable improved lower confinement regime (the I-Regime)[12, 13]. On the other hand, the presence of the impurity ions may impact the level of zonal flow[14], an important figure that suppresses the radial correlation length of the turbulent fluctuations, and thus regulates the turbulent transport[15].

The gyrokinetic simulation has been successfully used to understand the nonlinear turbulent transport of the particle, momentum and energy in both ion and electron channels, particularly originated from the drift wave instabilities such as ITG[15-22], ETG[23-25], TEM[26-28] and KBM[29-31]. In this work, we utilize the massively parallel 3D global particle simulation code GTC (Gyrokinetic Toroidal Code)[15] to study the drift wave instability and turbulence with the impurity ions. We implement a novel numerical scheme that is capable to solve the perturbed and flux averaged gyrokinetic Poisson equation with the impurity ions for arbitrary perpendicular wavelength. We verify these capabilities by a linear instability benchmark with the HD7 code[10] and simulating the correct zonal flow response with the impurity ions. Then, we show by the nonlinear simulation that the impurity ions can decrease the thermal ion heat diffusivity through reducing the linear drive, which favors the plasma confinement and is consistent with the current experimental observation[1-5].

This paper is organized as follows. In Section II, we describe the traditional approximation used in the GTC code to solve the perturbed Poisson equation with the impurity ions, which is suitable for the long wavelength modes. We then develop a new scheme to extend the traditional Poisson equation to cover arbitrary wavelength modes. In section III, we demonstrate the error of the traditional method and verify the linear ITG instability including impurities by comparing the GTC simulation with previous numerical results. We convert the flux averaged Poisson equation to a matrix problem in the large aspect-ratio limit to include the impurity ions properly in Section IV. In section V, we calculate the zonal flow response through the new zonal flow solver described in Section IV and show the agreement on the residual zonal flow level between the GTC simulation and the theoretical result. In section VI, we carry out the nonlinear simulation on the ITG mode with impurities, and investigate the effect of the impurities on the turbulent transport. Finally, the summary is made in Section VII.

II. New Poisson solver for impurity ions

The particle pushing algorithm for the impurity ions is identical to that for the thermal ions. The major complication in simulating impurity ions by a gyrokinetic code is about solving the gyrokinetic Poisson equation[16, 32, 33]. The gyrokinetic Poisson equation with impurity ions is given by

$$\frac{Z_i^2 n_{0i}}{T_i}\left(\Phi - \tilde{\Phi}_i\right) + \frac{Z_z^2 n_{0z}}{T_z}\left(\Phi - \tilde{\Phi}_z\right) + \frac{e^2 n_{0e}}{T_e}\Phi = \left(Z_i \bar{n}_i + Z_z \bar{n}_z - e n_{e,kinetic}\right), \qquad (1)$$

where Z is the particle charge, T is the equilibrium temperature, n_0 is the equilibrium density, e is the absolute value of electron charge, $\bar{n}$ is guiding center density, and $n_{e,kinetic}$ is non-adiabatic electron guiding center density. The subscripts i, e and z stand for ion, electron and impurity, respectively. Φ is the electric potential, and $\tilde{\Phi}$ denotes the second gyro-averaged potential[16],

$$\tilde{\Phi}_s(\mathbf{x}) = \frac{1}{2\pi}\int \bar{\Phi}(\mathbf{R})F_{M,s}\left(\mu, v_\parallel\right)$$
$$\times \delta(\mathbf{R} - \mathbf{x} + \rho)\,\mathrm{d}\,\mathbf{R}\,\mathrm{d}\,\mu\mathrm{d}v_\parallel\mathrm{d}\alpha, \qquad (2)$$

Where $F_{M,s}$ is the lowest order Maxwellian distribution for the particle species 's', α is the gyrophase. $\bar{\Phi}$ is defined as the first gyro-averaged potential,

$$\bar{\Phi}(\mathbf{R}) = \frac{1}{2\pi}\int \Phi(\mathbf{x})\delta\left(\mathbf{x} - \mathbf{R} - \rho\right)dxd\alpha. \qquad (3)$$

In the GTC code, the electrostatic Poisson equation (1) is solved through 4-point averaging method[32, 34] or the Padè approximation method[33]. Both methods are to find a discrete matrix to express $\tilde{\Phi}$ in terms of Φ to solve the differential-integral gyrokinetic Poisson equation in the real space. The differential equation is thus converted to a discrete difference equation and can be expressed in a compact matrix form. In the case of 4-point averaging method, the equation is given by

$$\left(\mathbf{M}_i + \mathbf{M}_z + \mathbf{D}\right)\delta\vec{\phi} = \delta\vec{\rho}. \qquad (4)$$

The one-dimensional arrays $\delta\vec{\phi}$ and $\delta\vec{\rho}$ represent the electric potential and charge density on the simulation grid points. The left hand side of the Poisson equation, the polarization response on every grid point due to the perturbative potential field $\delta\phi$, is expressed by the superposition of

the $\delta\phi$ on the adjacent grid points. This feature makes $\mathbf{M}_i$ and $\mathbf{M}_z$ sparse matrices. The matrix $\mathbf{D}$ is diagonal and induced by the adiabatic response of electrons. In the case of Padè approximation method, the discrete gyrokinetic Poisson equation takes another form

$$\left(\frac{\mathbf{U}_i}{\mathbf{L}_i}+\frac{\mathbf{U}_z}{\mathbf{L}_z}+\mathbf{D}\right)\delta\vec{\phi}=\delta\vec{\rho}, \tag{5}$$

Where $\mathbf{U}s$ and $\mathbf{L}s$ are sparse matrices.

In the long wave length limit, $k_\perp^2\rho_{th,s}^2\ll1$, we can expand $\tilde{\Phi}$ to the first order of $k_\perp^2\rho_{th,s}^2$, $\tilde{\Phi}\left(k_\perp^2\rho_{th,s}^2\right)=\left(1-k_\perp^2\rho_{th,s}^2+\cdots\right)\Phi$, and then the polarization response term becomes

$$\frac{Z_s^2 n_{0s}}{T_s}\left(\Phi-\tilde{\Phi}_s\right)\approx\frac{Z_s^2 n_{0s}}{m_s v_{s,th}^2}k_\perp^2\frac{m_s^2 v_{s,th}^2}{e^2 Z_s^2 B_0^2}\Phi\propto m_s n_{0s}, \tag{6}$$

where B_0 is the magnetic field strength at magnetic axis, $v_{th,s}$ is the thermal velocity for particle species s,

$$v_{th,s}=\sqrt{T_s/m_s}\,,\,\rho_{th,s}=\frac{m_s v_{th,s}}{Z_s B_0} \tag{7}$$

The polarization response term is proportional to the mass and equilibrium density for s=i, z. In this long wavelength limit, we can find

$$\mathbf{M}_z=\mathbf{M}_i\frac{m_z n_{0z}}{m_i n_{0i}}\,,\frac{\mathbf{U}_z}{\mathbf{L}_z}=\frac{\mathbf{U}_i}{\mathbf{L}_i}\frac{m_z n_{0z}}{m_i n_{0i}}. \tag{8}$$

Therefore, we can obtain the perturbative potential field by solving

$$\delta\vec{\phi}=\left(\frac{m_i n_{0i}\mathbf{M}_i}{m_z n_{0z}+m_i n_{0i}}+\mathbf{D}\right)^{-1}\delta\vec{\rho}, \tag{9}$$

in using the 4-point averaging method[32, 34], and solving

$$\delta\vec{\phi}=\left(\frac{m_i n_{0i}}{m_z n_{0z}+m_i n_{0i}}\mathbf{U}_i+\mathbf{L}_i\mathbf{D}\right)^{-1}\mathbf{L}_i\delta\vec{\rho}, \tag{10}$$

in the Padè approximation method[33]. Although the size of these matrices is large, their sparse features make it easy to inverse the matrices. When the impurity part is removed, or the density of

impurity n_{0_z} is set to 0, we recover the gyrokinetic Poisson equation for the single ion species case.

However, the above approximation is inaccurate when $k_\perp^2 \rho_{th,i}^2 \sim 1$, $k_\perp^2 \rho_{th,z}^2 \sim 1$, which can be the most unstable region for the drift wave instabilities. It is necessary to work out a scheme that can handle these short wavelength modes. We note that the calculation of $\mathbf{M}_i$ retains accurate when $k_\perp^2 \rho_{th,i}^2 \sim 1$. So we can use this method to calculate $\mathbf{M}_z$ similarly, which shares the same interface in the code as that for calculating $\mathbf{M}_i$. Knowing the particle mass, charge and equilibrium plasma profiles, we can obtain the gyrokinetic matrix for any kind of particle. Thus, the gyrokinetic Poisson equation with a second ion species can be solved directly by inversing the total gyrokinetic Poisson matrix

$$\delta\vec{\phi} = \left(\mathbf{M}_i + \mathbf{M}_z + \mathbf{D} \right)^{-1} \delta\vec{\rho}. \tag{11}$$

Note that we do not need to use the Padè approximation method[33] is that the quotient $\mathbf{U}/\mathbf{L}$ is not necessarily a sparse matrix, unless a proper truncation method is introduced so that the quotient $\mathbf{U}/\mathbf{L}$ is similar to $\mathbf{M}$. For the current purpose, it is sufficient to focus on the 4-point averaging method.

III. Verification of new Poisson scheme with impurity
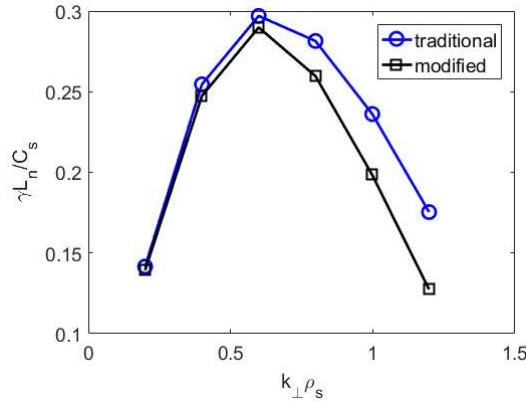

Figure 1 Linear growth rate in ITG instability with impurities v.s. perpendicular wave length for traditional gyrokinetic Poisson solver and new gyrokinetic Poisson solver, $\rho_s = \sqrt{2T_i / m_i}$.

The traditional gyrokinetic Poisson solver in the GTC code uses an approximate impurity response

$$\frac{Z_i^2 n_{0i}}{T_i} \frac{k_\perp^2 \rho_{th,i}^2}{1+k_\perp^2 \rho_{th,i}^2} \frac{m_z n_{0z}}{m_i n_{0i}} \phi = \frac{Z_z n_{0z}}{T_z} \frac{k_\perp^2 \rho_{th,z}^2}{1+k_\perp^2 \rho_{th,i}^2} \phi \tag{12}$$

to replace the actual impurity response $\frac{Z_z n_{0z}}{T_z} \frac{k_\perp^2 \rho_{th,z}^2}{1+k_\perp^2 \rho_{th,z}^2} \phi$. The error of this approximation for

short wavelengths, e.g. $k_\perp^2 \rho_{th,i}^2 \sim k_\perp^2 \rho_{th,z}^2 \sim 1$, can be significant, as is demonstrated by Fig. 1,

where $T_z = T_i$ is assumed for simplicity and the Carbon ion C^{6+} is used as the impurity since it

would be the major contaminant in the ITER plasmas[35]. Thus $\rho_{th,z} = \sqrt{3}/3 \rho_{th,i} < \rho_{th,i}$. The

above analysis shows that the approximate impurity response traditionally employed in the GTC is

smaller than its true value, and thus it will lead to a larger estimation for the potential ϕ. The

simulation result in Fig.1 indeed shows that the traditional gyrokinetic Poisson solver in GTC

gives a larger growth rate than the newly modified gyrokinetic Poisson solver, which is fully
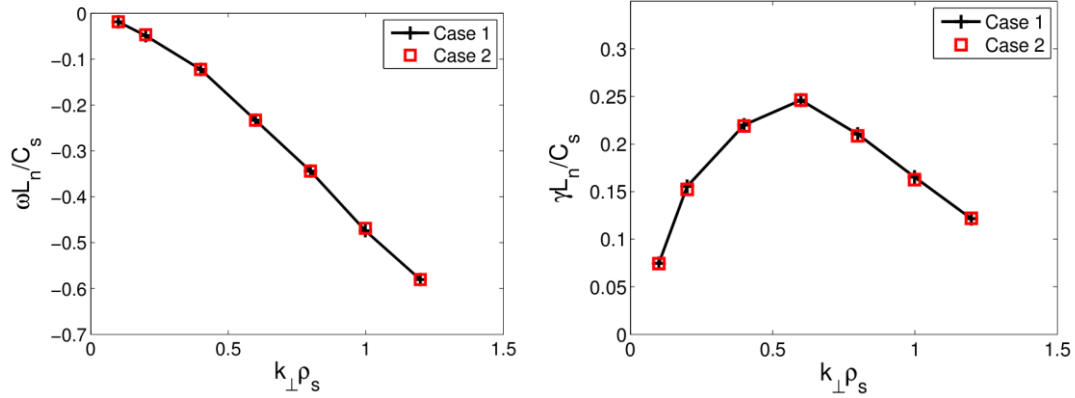
consistent with our analysis.

Figure 2 Code consistency check for linear ITG dispersion with different impurity portions. Case 1 80% ions, 20% impurities; case 2 20% ions, 80% impurities.

For both gyrokinetic Vlasov equation and gyrokinetic Poisson equation, the ion and the impurity are symmetric or exchangeable. The code must satisfy this symmetry, and when we exchange ion and impurity portion in the code, the simulation results should not have any change according to this physics understanding. We carry out an ITG simulation with impurities for two cases, with case 1: 80% thermal ions, 20% impurities, $m_i = m_{H^+}$, $Z_i = e$, $m_z = m_{C^{6+}}$,

$Z_z = 6e$, $\epsilon = 0.2$, $q = 2$, $\hat{s} = 1.5$, $L_{nz} = L_{ne}$, $\eta_e \equiv d\ln T_e / d\ln n_e \equiv L_{ne}/L_{Te} = 2.0$,

$T_z = T_i = T_e$, $\eta_i = 3.0$; and case 2: 20% thermal ions, 80% impurities, and all other parameters

exchanged between ions and impurity. The simulation results are shown in Fig.2, where the linear growth rate and frequency is identical for these two cases. This confirms the numerical symmetry between the ions and the impurities in the GTC code after this new method is implemented to solve the gyrokinetic system with both ions and impurities.
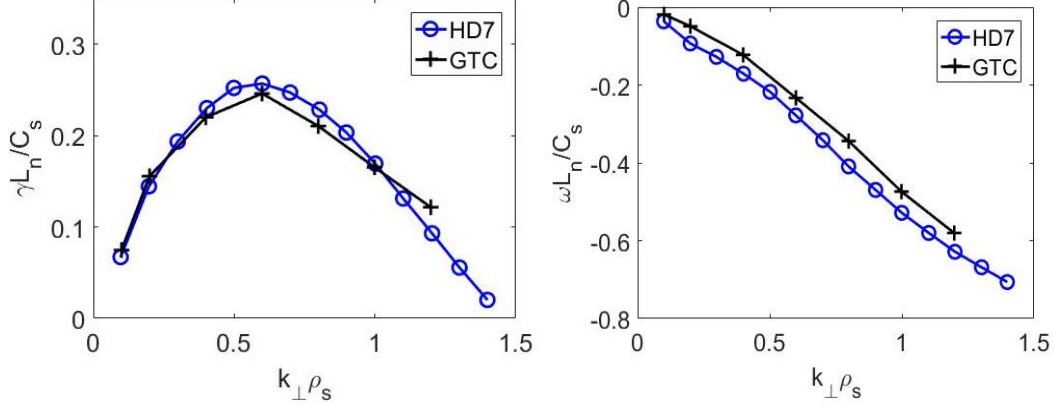

Figure 3 Linear dispersion of ITG from GTC simulation and HD7.

Next we verify this new capability in GTC by comparing the linear ITG dispersion with impurities with the gyrokinetic eigenvalue code HD7[10]. The simulation parameters are set as the same as case 1 in the preceding example. The simulation results in Fig.3, show that both linear frequency and growth rate from the GTC simulation are consistent with those from the HD7 simulation[10] in both value and tendency. Therefore, we can conclude that the new gyrokinetic Poisson solver can accurately address the impurity effect, even for the short wavelength modes with $k_\perp^2 \rho_{th,i}^2 \sim k_\perp^2 \rho_{th,z}^2 \sim 1$.

IV. New zonal solver

In order to carry out high fidelity turbulence simulation, it is important to confirm the accuracy of the zonal flow response. The formal derivation of zonal potential is through the flux surface average of the potential field,

$$\langle \phi \rangle = \frac{\oint J\phi d\theta d\zeta}{\oint J d\theta d\zeta}, \tag{13}$$

where $\phi = \delta\phi + \langle \phi \rangle$ is solved by the gyrokinetic Poisson equation. The electrons are mainly adiabatic in response to the perturbative $\delta\phi$. However, they are non-adiabatic in response to the zonal potential. Thus, the gyrokinetic Poisson equation can be split into two equations, the non-zonal gyrokinetic Poisson equation (1), and zonal gyrokinetic Poisson equation that is given by

$$\left\langle -\sum_{s=i,z} \frac{n_{s0} Z_s^2}{T_s} \frac{\rho_{th,s}^2 \nabla_\perp^2}{1-\rho_{th,s}^2 \nabla_\perp^2} \phi \right\rangle = \left\langle \rho_c \right\rangle. \tag{14}$$

Noting that $k_\perp^2 \rho_e^2 \ll 1$ and $\left\langle \rho_c \right\rangle = \left\langle Z_i n_i + Z_z n_z - n_{e,kinetic} \right\rangle$ is the flux surface averaged perturbed charge density. In the limit of large aspect ratio, to the lowest order the equation can be reduced tothe following equation[33],

$$\frac{\partial}{\partial \psi}\left(J(\psi)\left\langle g^{\psi\psi} \right\rangle \frac{\partial \langle \phi \rangle}{\partial \psi} \right) = \left(-\frac{T_i}{n_i Z_i^2} J(\psi)\left\langle \frac{1}{\rho_{th,i}^2} \right\rangle + \frac{T_i}{n_i Z_i^2} \frac{\partial}{\partial \psi} J(\psi)\left\langle g^{\psi\psi} \right\rangle \frac{\partial \langle \phi \rangle}{\partial \psi} \right) \langle \rho_c \rangle. \tag{15}$$

The zonal potential can be obtained by integrating the preceding equation numerically twice.

If the impurity ions are included in the equation, the preceding zonal equation (15) will end up with a fourth order differential equation, which is much more complicated to be solved. Moreover, the fourth order derivative on the zonal charge density introduces much larger numerical noise. Here we provide a better way to solve the zonal gyrokinetic Poisson equation.

In fact we can solve the flux surface averaged gyrokinetic Poisson equation by the matrix method that we just used for the perturbed gyrokinetic Poisson equation. The matrix form of (14) is

$$\left\langle \left(\frac{\mathbf{U}_i}{\mathbf{L}_i} + \frac{\mathbf{U}_z}{\mathbf{L}_z} \right) \vec{\phi} \right\rangle = \left\langle \vec{\rho}_c \right\rangle, \tag{16}$$

Where $\mathbf{U}$ is the matrix form of the operator $\left(n_0 Z^2 / T \right) \rho_{th,s}^2 \nabla_\perp^2$, and $\mathbf{L}$ is the matrix form of the operator $1 - \rho_{th,s}^2 \nabla_\perp^2$. Rather than multiply $\mathbf{L}$ on both sides of the preceding equation, we can directly combine the operator matrices acting on $\vec{\phi}$ into one single matrix. Define the total matrix $\mathbf{M}_t$ as $\mathbf{M}_t \equiv \mathbf{M}_i + \mathbf{M}_z = \mathbf{L}_i^{-1}\mathbf{U}_i + \mathbf{L}_z^{-1}\mathbf{U}_z$, the gyrokinetic Poisson equation can be further reduced to a linear matrix problem $\left\langle \mathbf{M}_t \right\rangle \left\langle \vec{\phi} \right\rangle = \left\langle \rho_c \right\rangle$, which assumes that the variation scales for the matrix $\mathbf{M}_t$ and the potential ϕ are different and has been shown to be accurate to the requisite order[33]. Although the matrix $\mathbf{M}_t$ is not necessarily a sparse matrix, the size of $\left\langle \mathbf{M}_t \right\rangle$ is only related to the number of grid points in radial direction, which is usually several hundreds. The size of this linear problem is within the tolerance range of modern computers. Many numerical libraries can be used to solve this problem, such as PetSc[36-38].

The matrix method introduced here has several advantages. First of all, this method expands the validity range of zonal solver from small gyro-radius limit to $k_\perp^2 \rho_{th,i}^2 \sim k_\perp^2 \rho_{th,z}^2 \sim 1$. Secondly, this method avoids the higher order derivatives of the array $\vec{\rho}_c$ and thus suppresses the associated numerical noises. Furthermore, it is symmetric in form for the ion species and thus easier to code additional ion species through the interface that constructs $\mathbf{L}_s^{-1}\mathbf{U}_s$, and the total matrix $\mathbf{M}_t$ is calculated by a simple summation.
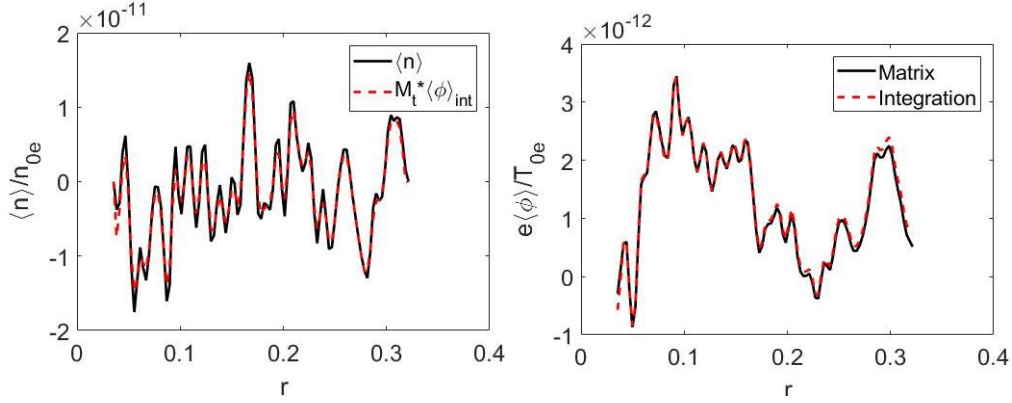
V. Verification of zonal solver

Figure 4 Comparison between zonal field solved by traditional integration method in GTC and new zonal solver.

Without the impurity ions, the traditional integration method is accurate enough to obtain the correct zonal field response, even for the short wavelength modes $k_\perp^2 \rho_i^2 \sim 1$. Thus for the case of one single ion species, the simulation result from the matrix method and traditional integration method should be identical, which is confirmed by the following test. At any time step of the simulation, we can record the zonal density $\langle \rho_c \rangle$ and the zonal field $\langle \phi \rangle_{int}$ solved by the integration method according to Eq. (14). We also denote $\langle \phi \rangle_M$ to the zonal field solved by the aforementioned matrix method. Then for this single species case, $\langle \phi \rangle_M = \langle \mathbf{M}_i \rangle^{-1} \langle \rho_c \rangle$. The matrix $\mathbf{M}_i$ does not change with time. The left panel of Fig.4 shows the plots of radial zonal density $\langle \rho_c \rangle$ and $\mathbf{M}_i \langle \phi \rangle_{int}$ at a certain time step. The consistency of two curves illustrates that $\mathbf{M}_i$ indeed corresponds to the differential operator that acts on $\langle \phi \rangle$, as shown in Eq. (14). On

the other hand, the radial structure of $\langle\phi\rangle_M$ calculated by the matrix method matches that of $\langle\phi\rangle_{int}$, as is plotted in the right panel in Fig.4. It is further observed that this consistency holds for any time step in the simulation.
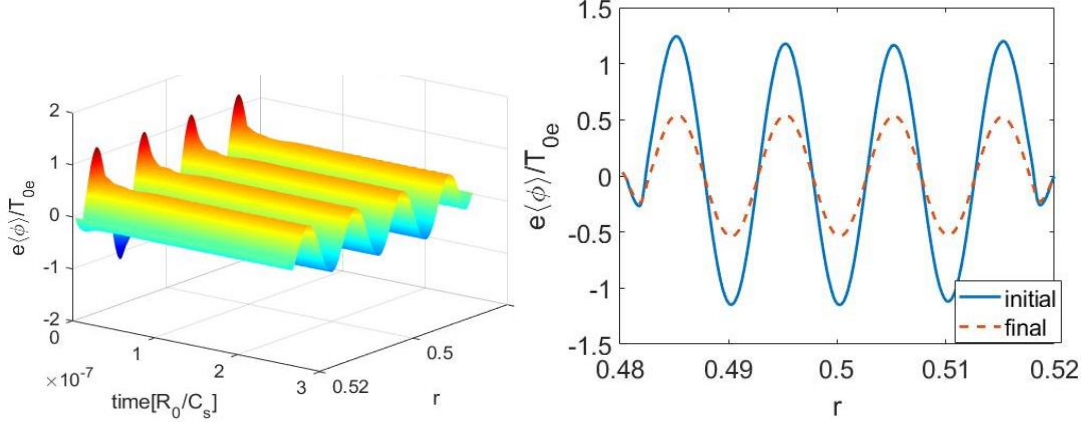

Figure 5 (a) Time evolution of zonal flow. (b) Initial zonal flow and stationary residual zonal flow.

To investigate the impurity effect on zonal flow and to verify the new zonal field solver, we studied the classical Rosenbluth-Hinton zonal flow residual problem[39] and have simulated the residual zonal flow response with impurities in the collisionless limit. Initially we load an external radial potential field to excite radial density fluctuation. After a certain time step which is set as t=0, the external field is removed and the time history of zonal flow is measured. Under the collisionless condition, the zonal flow damps away because of the shielding of the neoclassical polarization. After several bounce times, the zonal flow reaches a steady state. The time evolution of the radial structure of the zonal flow is shown in the left panel. We choose the initial radial zonal flow at t=0 and steady zonal flow structure to calculate the residual zonal flow level R_{ZF}.

Analytical and numerical solutions in terms of the critical parameters, such as the safety factor q, radial wave vector k_r and inverse aspect-ratio ε, are presented in large aspect-ratio limit to calculate the residual zonal flow level R_{ZF}[14, 40, 41]. The residual zonal flow level is given by the following formula

$$R_{ZF} = \frac{\sum_{\alpha} g_{\alpha}\chi_{\alpha,cl}}{\sum_{\alpha} g_{\alpha}\left(\chi_{\alpha,cl}+\chi_{\alpha,nc}\right)}, \alpha = i,e,z, \tag{17}$$

where $g_e = 1$, $g_i = T_i/T_e\left(1-f_z\right)$, $g_z = T_z/T_e Z_z f_z$, f_z is the fraction of impurity ions,

$f_z = 1 - \dfrac{n_i}{n_e}$ and $\chi_{\alpha,cl}$, $\chi_{\alpha,nc}$ is the classical and neo-classical polarization of the particle,

$$\chi_{s,cl} = 1 - \left\langle \Gamma_0\left(k_\perp^2 \rho_{th,s}^2\right)\right\rangle, \tag{18}$$

$$\chi_{s,nc} = \left\{ \frac{1}{1.83\epsilon^{3/2}k_r^2\rho_{\theta,s}^2} + \left[1 + \frac{\sqrt{8\epsilon}}{\pi}\Gamma_{tr}' + \left(1 - \frac{\sqrt{8\epsilon}}{\pi}\right)\Gamma_p'\right]\frac{1}{1+k_r^2\rho_{th,s}^2} \right. $$
$$\left. + \sqrt{\frac{\pi^3}{2}}k_r\rho_{th,s} \times \left[1 + \frac{\sqrt{8\epsilon}}{\pi}\Gamma_{tr} + \left(1 - \frac{\sqrt{8\epsilon}}{\pi}\right)\Gamma_p\right]\frac{k_r^2\rho_{th,s}^2}{1+k_r^2\rho_{th,s}^2} \right\}^{-1}, \tag{19}$$

where

$$\rho_{\theta,s} = \rho_{th,s}q/\epsilon,\ \Gamma_{tr} \approx \frac{0.916}{\sqrt{\pi\epsilon}k_r\rho_{\theta,s}},\ \Gamma_p = \frac{1}{2\sqrt{2\pi\epsilon}k_r\rho_{\theta,s}}, \tag{20}$$

and $\Gamma_{tr}' = 2\Gamma_{tr}/\pi$, $\Gamma_p' = 2\Gamma_p/\pi$.
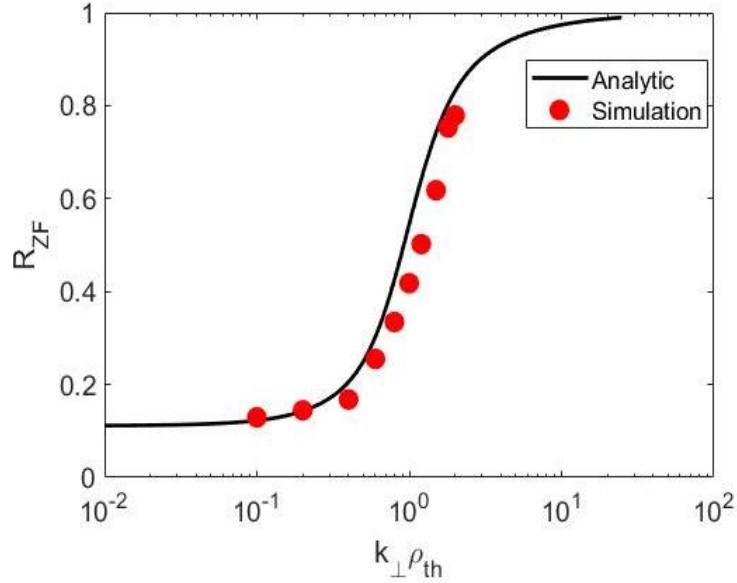

Figure 6 Residual zonal flow dependency on radial wave length.

Given $\epsilon = 0.2$, $q = 1.4$, $T_i = T_z = T_e$, the $k_\perp\rho_{th,i}$ dependency of R_{ZF} is shown in Fig.6. The $k_\perp\rho_{th,i}$ parameter ranges from 0.2 to 2.0, where is within the effective range of the Padè approximation employed in the zonal flow solver. In the small gyro-radius limit, the residual zonal flow approaches to the Rosenbluth-Hinton constant. In the finite gyro-radius limit, $k_\perp\rho_{th} \sim 1$, the

zonal flow is not shielded at all and R_{ZF} approaches to 1. The particle simulation by GTC can produce accurately these two analytic limits, with various ratio $\rho_{th,z} / \rho_{th,i}$. So the new zonal field solver with impurities by the matrix method can produce the correct zonal flow response in a wide range from $k_\perp \rho_{th,i} \sim k_\perp \rho_{th,z} \ll 1$ to $k_\perp \rho_{th,i} \sim k_\perp \rho_{th,z} \sim 1$.
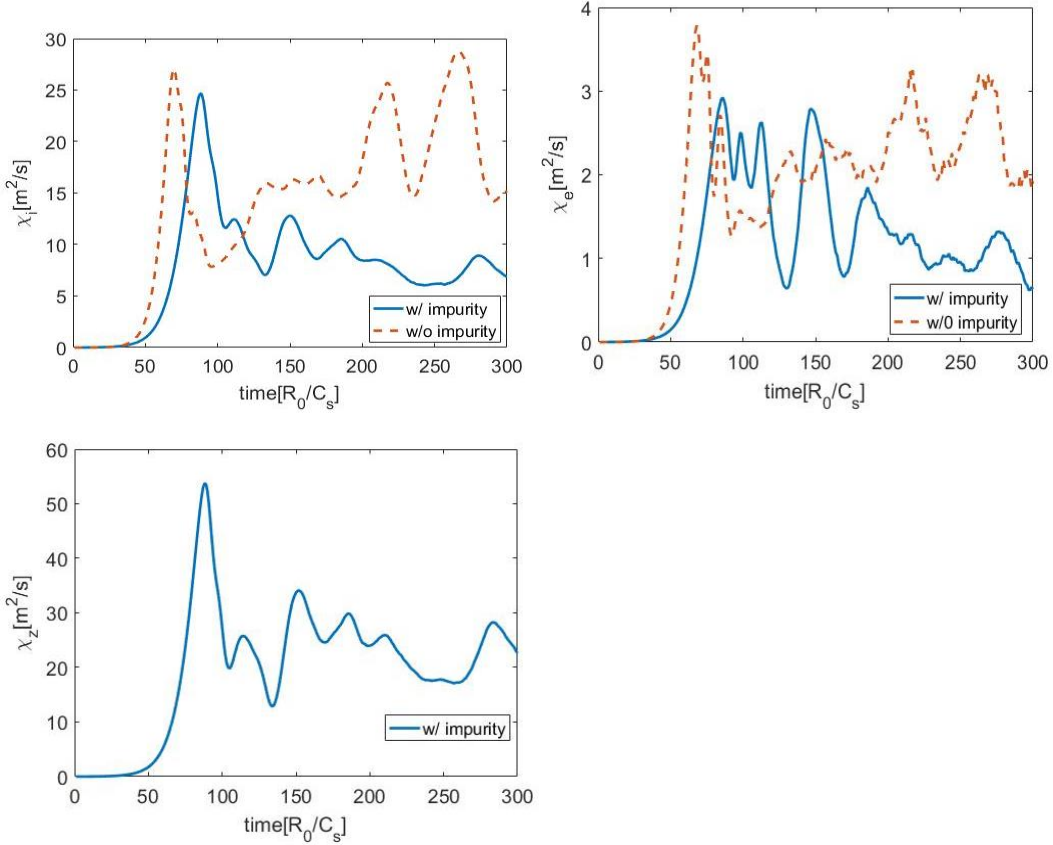

Figure 7 Volume-averaged heat diffusivity time evolution for (a) ions (b) electrons (c) impurity ions. The red(blue) line is from the simulation without(with) impurity ions.

VI. Nonlinear ITG simulation with impurities

To investigate the effect of impurity ions on the turbulent ion heat diffusivity, we carry out two nonlinear GTC simulations after the improved gyrokinetic Poisson and zonal flow solver is implemented and verified. The simulations use the Cyclone base case parameters[42], on the reference surface $\epsilon = r / R_0 = 0.18$, the local parameters are $n_i = n_e$, $T_i = T_e$, $\eta_e = 3.1$, $q = 1.4$, $\hat{s} = 0.78$, $R / L_T = 6.9$, with one containing only ions and electrons, and the other containing an additional impurity ions C^{6+}. In order to see a significant role for the impurities we set the impurity fraction $f_z = 0.2$. We also assume that the impurities are completely thermalized

by the ions through collisions, i.e., $T_z = T_i$. In Fig. 7, we show the time history of the heat diffusivity for these two simulations. In the nonlinear phase, the presence of the impurity ions significantly decreases the saturation level of the heat diffusivity for both ions and electrons. According to Eq. (17) and the parameters we have used, the residual zonal flow level is only slightly lower when the impurity ions are included. Thus the change in the regulation effect on thermal transport by the zonal flow is small. Note that the linear growth rate is lower in the simulation with impurity ions. From Fig. 7, one can estimate $\gamma_z = 0.57 C_s / R_0$, $\gamma_{w/o\, z} = 0.83 C_s / R_0$. So we can conclude that the difference of the turbulent thermal diffusivity for these two cases mainly results from the change in linear growth rate, i.e., the linear driving force for the turbulence. The impurity ions play a damping role for the turbulence, which can help improve the confinement of tokamaks. This can be used to explain the current experimental observations, where external impurity injection can lead to long wavelength turbulence suppression, confinement improvement and ion thermal diffusivity reduction[1-5].

VII. Summary

We have implemented a new numerical scheme in the GTC code to solve multiple-species gyrokinetic Poisson equation and have extended the validity range of the gyrokinetic Poisson solver and the zonal field solver in the GTC code with impurity ions from the long wavelength $k_\perp \rho_{th,i} \sim k_\perp \rho_{th,z} \ll 1$ to the short wavelength $k_\perp \rho_{th,i} \sim k_\perp \rho_{th,z} \sim 1$. For the Poisson solver, we have implemented an interface to calculate the 4-point averaging matrix for any particle species. The total matrix for the linear Poisson equation is the summation of each individual species matrix. The benchmark of the ITG with impurity ions between GTC and HD7 shows the validity of this scheme. As for the zonal flow solver, we replace the conventional integration method with a new matrix method based on the Padè approximation so that we can incorporate the impurity effect conveniently and accurately. In the case where only thermal ions are included, we have demonstrated the equivalence of the matrix method and the integration method. The new zonal field solver is further verified by calculating correctly the residual zonal flow level predicted by the asymptotic theory when the impurity ions are included. The comparison of nonlinear simulations with and without impurity shows that the impurity ions can decrease the thermal ion heat diffusivity through reducing the linear drive, which is consistent with the current experimental observation[1-5] and shows that the impurities can help improve the heat confinement of tokamaks.

Acknowledgements

References

1. A. M. Messiaen, J. Ongena, U. Samm, et al., Physical Review Letters **77** (12), 2487-2490 (1996).
2. G. McKee, K. Burrell, R. Fonck, et al., Physical Review Letters **84** (9), 1922-1925 (2000).
3. M. Murakami, G. R. McKee, G. L. Jackson, et al., Nuclear Fusion **41** (3), 317 (2001).
4. G. P. Maddison, M. Brix, R. Budny, et al., Nuclear Fusion **43** (1), 49 (2003).
5. K. W. Hill, S. D. Scott, M. Bell, et al., Physics of Plasmas **6** (3), 877-884 (1999).
6. B. Coppi, H. P. Furth, M. N. Rosenbluth and R. Z. Sagdeev, Physical Review Letters **17** (7), 377-379 (1966).
7. W. M. Tang, R. B. White and P. N. Guzdar, The Physics of Fluids **23** (1), 167-173 (1980).
8. J. Q. Dong and W. Horton, Physics of Plasmas **2** (9), 3412-3419 (1995).
9. D. K. Bhadra, The Physics of Fluids **18** (3), 380-383 (1975).
10. H. Du, Z.-X. Wang, J. Q. Dong and S. F. Liu, Physics of Plasmas **21** (5), 052101 (2014).
11. B. Coppi and T. Zhou, Physics of Plasmas **19** (1), 012302 (2012).
12. R. M. McDermott, B. Lipschultz, J. W. Hughes, et al., Physics of Plasmas **16** (5), 056103 (2009).
13. D. G. Whyte, A. E. Hubbard, J. W. Hughes, et al., Nuclear Fusion **50** (10), 105005 (2010).
14. W. Guo, L. Wang and G. Zhuang, Nuclear Fusion **57** (5), 056012 (2017).
15. Z. Lin, T. S. Hahm, W. W. Lee, et al., Science **281** (5384), 1835 (1998).
16. W. W. Lee, The Physics of Fluids **26** (2), 556-562 (1983).
17. W. W. Lee and W. M. Tang, The Physics of Fluids **31** (3), 612-624 (1988).
18. P. Angelino, X. Garbet, L. Villard, et al., Physical Review Letters **102** (19), 195002 (2009).
19. S. E. Parker, W. W. Lee and R. A. Santoro, Physical Review Letters **71** (13), 2042-2045 (1993).
20. R. D. Sydora, V. K. Decyk and J. M. Dawson, Plasma Physics and Controlled Fusion **38** (12A), A281 (1996).
21. W. Horton, Reviews of Modern Physics **71** (3), 735-778 (1999).
22. Y. Chen and S. E. Parker, Physics of Plasmas **14** (8), 082301 (2007).
23. Z. Lin, I. Holod, L. Chen, et al., Physical Review Letters **99** (26), 265003 (2007).
24. Y. Idomura, S. Tokuda and Y. Kishimoto, Nuclear Fusion **45** (12), 1571 (2005).
25. W. Dorland, F. Jenko, M. Kotschenreuther and B. N. Rogers, Physical Review Letters **85** (26), 5579-5582 (2000).
26. Z. Lin, Y. Nishimura, Y. Xiao, et al., Plasma Physics and Controlled Fusion **49** (12B), B163 (2007).
27. J. Lang, S. E. Parker and Y. Chen, Physics of Plasmas **15** (5), 055907 (2008).
28. Y. Xiao and Z. Lin, Physical Review Letters **103** (8), 085004 (2009).
29. W. M. Tang, J. W. Connor and R. J. Hastie, Nuclear Fusion **20** (11), 1439 (1980).
30. T. F. Tang, X. Q. Xu, C. H. Ma, et al., Physics of Plasmas **23** (3), 032119 (2016).
31. L. J. Zheng and M. Tessarotto, Physics of Plasmas **1** (12), 3928-3935 (1994).
32. Z. Lin and W. W. Lee, Physical Review E **52** (5), 5646-5652 (1995).
33. Y. Xiao, I. Holod, Z. Wang, et al., Physics of Plasmas **22** (2), 022516 (2015).
34. W. W. Lee, Journal of Computational Physics **72** (1), 243-269 (1987).
35. ITER Physics Basis Editors, ITER Physics Expert Group Chairs and Co-Chairs, ITER Joint

Central Team and Physics Integration Unit, Nuclear Fusion **39** (12), 2137 (1999).

36. S. Balay, S. Abhyankar, M. F. Adams, et al., http://www.mcs.anl.gov/petsc.

37. S. Balay, S. Abhyankar, M. F. Adams, et al., Report No. ANL-95/11 - Revision 3.8, 2017.

38. S. Balay, W. D. Gropp, L. C. McInnes and B. F. Smith, in *Modern Software Tools in Scientific Computing*, edited by E. Arge, A. M. Bruaset and H. P. Langtangen (Birkhäuser Press, 1997), pp. 163-202.

39. M. N. Rosenbluth and F. L. Hinton, Physical Review Letters **80** (4), 724-727 (1998).

40. Y. Xiao, Massachusetts Institute of Technology, 2007.

41. L. Wang and T. S. Hahm, Physics of Plasmas **16** (6), 062309 (2009).

42. A. M. Dimits, G. Bateman, M. A. Beer, et al., Physics of Plasmas **7** (3), 969-983 (2000).